PAPER • OPEN ACCESS

Tailoring dielectric permittivity of epitaxial Gd-doped CeO_{2-x} films by ionic defects

To cite this article: A Palliotto *et al* 2024 *J. Phys. Energy* **6** 025005

View the article online for updates and enhancements.

Journal of Physics: Energy

PAPER

Tailoring dielectric permittivity of epitaxial Gd-doped CeO$_{2-x}$ films by ionic defects

A Palliotto[1] , Y Wu[1], A D Rata[2] , A Herklotz[2] , S Zhou[3] , K Dörr[2], P Muralt[4] and D-S Park[1,*]

[1] Department of Energy Conversion and Storage, Technical University of Denmark, 2800 Kgs Lyngby, Denmark
[2] Institut für Physik, Martin-Luther-Universität Halle-Wittenberg, 06099 Halle, Germany
[3] Helmholtz-Zentrum Dresden-Rossendorf, Institute of Ion Beam Physics and Materials ResearchBautzner Landstraße 400, 01328 Dresden, Germany
[4] Institute of Materials, Swiss Federal Institute of Technology—EPFL, 1015 Lausanne, Switzerland
[*] Author to whom any correspondence should be addressed.

E-mail: daepa@dtu.dk

Abstract

Engineering materials with highly tunable physical properties in response to external stimuli is a cornerstone strategy for advancing energy technology. Among various approaches, engineering ionic defects and understanding their roles are essential in tailoring emergent material properties and functionalities. Here, we demonstrate an effective approach for creating and controlling ionic defects (oxygen vacancies) in epitaxial Gd-doped CeO$_{2-x}$ (CGO)(001) films grown on Nb:SrTiO$_3$(001) single crystal. Our results exhibit a significant limitation in the formation of excess oxygen vacancies in the films during high-temperature film growth. However, we have discovered that managing the oxygen vacancies in the epitaxial CGO(001) films is feasible using a two-step film growth process. Subsequently, our findings show that manipulating excess oxygen vacancies is a key to the emergence of giant apparent dielectric permittivity (e.g. $\varepsilon' \approx 10^6$) in the epitaxial films under electrical field control. Overall, the strategy of tuning functional ionic defects in CGO and similar oxides is beneficial for various applications such as electromechanical, sensing, and energy storage applications.

1. Introduction

Tuning parameters in material engineering are often correlated. For example, the presence of charged point defects in the lattice of a material leads to significant internal strain due to atomic and/or electronic rearrangement, as well as changes in local or macroscopic symmetry [1–5]. These defects have been extensively employed as a critical component to manipulate the properties of functional oxide materials for their device applications such as resistive random-access memories, conducting electrolytes, and solid-state fuel cells [2, 6–8]. Thus, effective control of such dynamic ionic defects and understanding their role are crucial in functionalizing highly tunable oxide materials.

The introduction of aliovalent cation into fluorite oxides deliberately arrange anion vacancies, which causes deviations from the typical fluorite structure and gives rise to multiple intermediate elastic/electronic phases [9]. For instance, when the Ce^{4+} ions of CeO$_2$ are replaced with rare-earth 3+ cations (e.g. rare-earth element, R = La, Sm, Nd, Gd), it induces the creation of oxygen vacancies (V$_O$) as compensating defects to maintain charge neutrality. In these systems, it is believed that their electromechanical properties are strongly coupled with the rate-dependence of dynamic V$_O$ under electric field. Recently, exceptionally large electromechanical effects in the doped fluorites have been found, prominently appearing at low frequencies ($f < 10$ Hz) [1, 10]. Similar large electrostrictive effects were also found in nonlinear materials such as bismuth oxides (Bi$_7$Nb$_{2-x}$Y$_x$O$_{2-2/x}$) and halide perovskites (MAPbI$_3$) [11, 12]. These materials with nonlinear properties under field excitation typically exhibit intrinsic relative permittivity denoted as ε_r in the range of approximately 20–70, particularly at relatively high frequencies (>1 kHz). This is generally

determined by applying low electric fields, typically a few kilovolts per centimeter or even lower. The permittivity values for many nonlinear oxides and similar systems can be found in [13]. However, under sufficiently high electric fields, dynamic V_O redistribution can significantly affect the apparent mechanical and electric displacement of the systems. This arises from macroscopic oxygen variations and charge rearrangement [1]. The dielectric permittivity is a key property of electromechanical coupling where the polarization (P)-induced electrostrictive strain is expressed by $x = QP^2 = M(P/\varepsilon)^2$, where Q and M are the polarization-induced and electric field-induced electrostrictive coefficient, respectively [14]. Hence, it is essential to understand the correlation between the role of ionic defects and the corresponding relaxation behavior of apparent dielectric permittivity under electric fields.

Subsequently, a recent study showed the potential for generating substantial piezoelectricity in centrosymmetric cubic Gd-doped CeO_{2-x} (CGO), which nominally forbids piezoelectricity. This achievement was made possible by utilizing the piezoelectric effect induced by a static electric field [1]. The control of the V_O dynamics within a polycrystalline CGO film was achieved by simultaneously applying static (E_{DC}) and driving alternating (E_{AC}) fields. The size of the induced piezoelectric effect of the CGO is remarkably large with apparent coefficients of $\approx$100 000 pm V^{-1} at low frequencies, while the relatively high-frequency piezoelectric coefficient is $\approx$100 pm V^{-1} at $f = 1$ kHz. In parallel, it was found that the apparent dielectric permittivity ($\varepsilon = \partial P/\partial E_{AC}$) of the system shows a strong frequency dependence, dominated by the static field-forced migration (/hopping) of V_O. These results directly indicate that the impact of dynamic V_O under the applied field strongly governs both the dielectric and electromechanical properties of the system.

The electromechanical properties of CGO have been reported for polycrystalline materials including particles, ceramics, and textured microscale films for their potential electromechanical applications such as actuators and sensors [1, 11, 13, 15]. These materials inherently possess microstructural characteristics such as varying grain sizes, shapes, orientations, and grain boundary density. These characteristics significantly influence ionic motion and transport within the system. Often, they lead to non-uniform or diminished dielectric and electromechanical properties, making it challenging to establish a direct correlation between field-induced V_O dynamics and the resulting electrical polarization of the system.

To gain a clearer understanding of these correlated effects, utilizing single-crystalline CGO film materials is a straightforward approach in conjunction with optimizing epitaxial film growth parameters such as growth temperature and background gas pressure. Tuning the strain of epitaxial CGO films has been effectively evoked by varying the thickness of the films on distinct underlying materials/substrates and external dopant concentration [16–18]. However, some of the research has shown that there is no significant change in the strain of CGO films (thickness > 50 nm) grown at high temperature (e.g. $T > 500\,^\circ$C) although the films were prepared under different oxygen background pressure [19, 20]. This indicates the limited control of V_O contents in the employed film growth regime. To the best of our knowledge, there has been no direct investigation yet on the control of V_O contents and the associated strain effect in epitaxial CGO films. This exploration is beyond the compensating effect of V_O concentration in the CGO system, typically determined by Gd doping concentration. Therefore, understanding the growth characteristics of epitaxial CGO films is paramount to clarify the role of the compensating and excess V_O contents for exploring and controlling the strain effect and correlated functional properties.

Here, we demonstrate the influence of growth conditions of epitaxial CGO(001) films on Nb-doped $SrTiO_3$(001) single crystal with the aim of controlling ionic V_O defects. Our results reveal a significant limitation to the oxygen reduction within the epitaxial CGO films during high-temperature growth (e.g. $T = 700\,^\circ$C) regardless of the oxygen background pressure. However, an effective control of Vo contents in epitaxially grown films is achievable by employing a two-step growth strategy—an initial growth of CGO buffer layer at high temperature ($T = 700\,^\circ$C), followed by a subsequent low-temperature ($T = 400\,^\circ$C) growth of CGO film. Subsequently, we show that manipulating the excess V_O in CGO is a crucial factor in generating high dielectric permittivity under electric field control.

2. Experimental

2.1. Film fabrication

Epitaxial CGO films were grown on TiO_2-terminated Nb(0.5 at.%)-doped $SrTiO_3$ (Nb:STO)(001) substrates [$5 \times 5 \times 0.5$ (z) mm^3 size] by using pulsed laser deposition (PLD) (a KrF excimer laser, $\lambda = 248$ nm). For film growth, a CGO (Gd: 20%) ceramic target was used and the target-to-substrate distance was fixed at 4.5 cm. All the films were grown by a laser energy fluence of approximately 1.5 J cm^{-2} with a repetition rate of 3 Hz. Two different growth processes were employed: (i) 700 $^\circ$C for one-step growth and (ii) 700 $^\circ$C for the CGO buffer layer and 400 $^\circ$C for the main film in a two-step growth. The V_O contents in the grown samples were controlled by adjusting oxygen partial pressure ($P_O = 1 \times 10^{-1}$ to 7×10^{-6} mbar). After the

film growth, all the film samples were cooled down to room temperature at the same P_O used during growth. For verification work, SrRuO$_3$ (SRO) layers (~15 nm-thick) grown at 700 °C in $P_O = 1 \times 10^{-1}$ mbar were employed prior to CGO film growth (see the supplementary information).

2.2. Sample characterizations

Structural properties of the grown CGO films were investigated using an X-ray diffraction (XRD) analysis (Rigaku, SmartLab X-ray Diffractometer) at room temperature using Cu-$K\alpha$1 radiation ($\lambda = 1.54056$ Å). Atomic force microscopy (AFM) was employed to study the surface topology of the Nb:STO and grown CGO films. AFM topology was analyzed using a Bruker Dimension Icon. ScanAsyst—Tapping mode was used with a ScanAsyst-Air tip (0.4 N m^{-1}). The scanned size was 5×5 μm^2 with a 1 Hz scan rate. X-ray photoemission spectroscopy (XPS) measurements were performed under ultra-high vacuum (base pressure $= 3 \times 10^{-11}$ mbar) using an ESCALAB Xi+ x-ray photoelectron spectrometer microprobe (Thermo Fisher Scientific, Ease Grinstead, UK) and a monochromatic Al Kα x-ray source ($h\nu = 1486.6$ eV). The emitted photoelectrons from the surface of the samples were collected with a take-off angle of 90°. The binding energy scale was calibrated to the C 1s core-level peak at the binding energy of 284.5 eV with an overall energy resolution of 470 meV. The XPS spectra were fitted using a Tougaard background subtraction and Voigt line shape. Compositional ratios of the elements (Ce, Gd, and O) in the films were determined after correcting for the inelastic mean free paths of the emitted photoelectrons via the TPP-2M formula [21] and by applying a Scofield photoionized cross-section [22]. The impedance measurements were performed by using a Solartron 1255B Frequency Response Analyzer and a 1296 Dielectric Interface. The complex impedance (Z^*) of the film samples was measured by applying alternating voltages (V_{AC}) as

$$V_{AC} = Z^*(\omega) I, \tag{1}$$

$$Z^*(\omega) = Z'(\omega) + jZ''(\omega), \tag{2}$$

where I is the measured current, Z' and Z'' are the real and imaginary parts of complex impedance, respectively. The complex permittivity (ε^*) of the samples can be derived from the relation:

$$\varepsilon^*(\omega) = \varepsilon'(\omega) + i\varepsilon''(\omega) = \frac{1}{i\omega C_0 Z^*(\omega)}, \tag{3}$$

where $\varepsilon'(\omega)$ and $\varepsilon''(\omega)$ are the real part and imaginary part of the permittivity, respectively, and C_0 is the vacuum capacitance. Both $\varepsilon'(\omega)$ and $\varepsilon''(\omega)$ were extracted from the impedance in a conventional way as the following equations:

$$\varepsilon'(\omega) = -\frac{d}{\omega A \varepsilon_0} \frac{Z''(\omega)}{Z'(\omega)^2 + Z''(\omega)^2}, \tag{3.1}$$

$$\varepsilon''(\omega) = \frac{d}{\omega A \varepsilon_0} \frac{Z'(\omega)}{Z'(\omega)^2 + Z''(\omega)^2}, \tag{3.2}$$

where d is the thickness of CGO film, A is the electrode area, and ε_0 is the vacuum permittivity.

To fit the dielectric spectra of the CGO film samples, the two main dielectric relaxation processes across the frequency range are given as:

$$\varepsilon_T^* = \varepsilon_{MW}^* + \varepsilon_U^*, \tag{4}$$

The real part (ε'_{MW}) and imaginary part (ε''_{MW}) of the complex Maxwell–Wagner (MW) functions can be expressed by:

$$\varepsilon_{MW}^* = \varepsilon'_{MW} + j\varepsilon''_{MW}, \tag{5}$$

$$\varepsilon'_{MW} = \varepsilon_\infty + \frac{\varepsilon_s - \varepsilon_\infty}{1 + \omega^2 \tau^2}, \tag{5.1}$$

$$\varepsilon''_{MW} = \frac{(\varepsilon_s - \varepsilon_\infty)\omega\tau}{1 + \omega^2 \tau^2} + \frac{\sigma_{DC}}{\varepsilon_0 \omega}. \tag{5.2}$$

The real part (ε'_U) and imaginary part (ε''_U) of the complex universal dielectric relaxation (UDR) functions can be described by a power law as:

$$\varepsilon_U^* = \varepsilon'_U + j\varepsilon''_U, \tag{6}$$

$$\varepsilon'_U = \left(\frac{\sigma_U}{\varepsilon_0}\right) \tan\left(\frac{s\pi}{2}\right) \omega^{-(1-s)}, \tag{6.1}$$

$$\varepsilon_U'' = \left(\frac{\sigma_U}{\varepsilon_0}\right)\omega^{-(1-s)}. \tag{6.2}$$

3. Results and discussion

To investigate the effect of V_O on the lattice strain in grown films, we prepared CGO film samples by PLD with different oxygen partial pressures, $P_O = 1 \times 10^{-1}$ mbar, 1×10^{-2}, 5×10^{-3}, 5×10^{-4}, and 7×10^{-6} mbar. Note that the $P_O = 7 \times 10^{-6}$ mbar was the base pressure at 700 °C for the PLD chamber used for film growth (see the Experimental section). All the CGO films were epitaxially grown on TiO$_2$-terminated Nb:STO(001) single crystal at 700 °C and exhibited atomically flat surfaces (figure 1(a)). The thickness of the grown films kept being similar in the range of ∼78 to ∼85 nm, where the films are fully relaxed without significant epitaxial constraint in the given growth condition (see figures 1(b) and (c)).

Figure 1(d) shows XRD θ–2θ patterns of the CGO films as a function of P_O, grown on Nb:STO(001). We observed no significant change in the CGO(002) peak positions and reciprocal space map (RSM) CGO(024) reflections of the grown films with different P_O (figures 1(d) and (e)). This suggests no prominent variations in the out-of-plane strain ($x_z < +0.018\%$) of the films. This was calculated by using the c-lattice parameter (5.40 ± 0.01 Å) of the CGO film grown at 1×10^{-1} mbar. These results indicate that changing the oxygen partial pressure in the chamber seems not to influence the films with the P_O. To further confirm this, new films were grown by similar reduced conditions (e.g. $T = 700$ °C and $P_O = 5 \times 10^{-4}$ mbar) at different PLD chambers in different places (MLU, Germany). Similarly, the results show no significant change in the CGO(002) peak position of the films grown with other P_O (figure 1(f)). These results were confirmed in different labs: (i) a CGO(001) film grown on Nb:STO(001) at 1×10^{-1} mbar at Technical University of Denmark, (ii) a CGO(001) film grown on Nb:STO(001) at $P_O = 1 \times 10^{-1}$ mbar at Martin-Luther-Universität (MLU), and (iii) a CGO(001) film grown on Nb:STO(001) at $P_O = 5 \times 10^{-4}$ mbar at MLU. The change of P_O during the high-temperature growth and cooling process does not cause any significant variation in the lattice constant, from which we can infer that the pressure in the given range does not impact on the V_O concentration in the grown films, and that the deviation from V_O concentration is small. It is well-documented that oxygen-deficient ceria and ceria-based materials have a propensity to readily react and store oxygen [23, 24]. Consequently, the ability to manipulate the content of oxygen vacancies in the doped films is restricted under the prevailing high-temperature film growth conditions that encourage oxidation activities.

To alleviate such an oxidation effect observed during high-temperature film growth, we employed a two-step film growth: (i) an initial growth of oxidized CGO buffer layer (approximately 10 nm thickness) at $T = 700$ °C and (ii) the subsequent 100 nm-thick film growth at $T = 400$ °C as schematically illustrated in the inset of figure 2(a). The assumption is that the low-temperature growth can minimize the oxidation during and after CGO film growth assuming that the oxidation in oxides typically becomes significant above ∼500 °C with the surrounding oxygen environment [25]. Figure 2(a) exhibits the XRD θ–2θ patterns of the CGO films on TiO$_2$-terminated Nb:STO(001) as a function of P_O, using the two-step growth technique. The high-temperature CGO buffer (∼10 nm thick) was grown on Nb:STO(001) with a positive in-plane strain of $\varepsilon_x \approx +1.8\%$ and a negative out-plane strain of average $\varepsilon_z \approx -0.5\%$, confirmed by RSM. A corresponding Poisson coefficient of ≈0.31 was measured for the elastic distortion of the epitaxial thin film, which is consistent with the reported values [26]. The biaxial lattice strain occurs due to the lattice mismatch between CGO ($a_{[100]} = 5.425$ Å) and Nb:STO ($a_{[110]} = 5.52$ Å).

The low-temperature (400 °C) CGO films were grown by varying P_O after the growth of a consistent high-temperature CGO buffer layer ($T = 700$ °C in $P_O = 0.1$ mbar). The thickness of the films remained constant at about 100–120 nm. Notably, we observed that the oxidized CGO buffer layer effectively promoted the epitaxial growth of CGO(001) films even at the low temperature. The epitaxial relationship between the CGO and Nb:STO was found to be $[110]_{CGO}||[100]_{STO}$ and $[001]_{CGO}||[001]_{STO}$ as schematically shown in figure 2(c) and supplementary figure S1. Moreover, clear shifts in the CGO film peaks toward lower 2θ angles when the P_O decreased to 5×10^{-3} mbar, revealing the c-lattice elongation of the CGO films with lower P_O (figure 2(a)). RSM further confirms that the in-plane lattice of the CGO film (approximately 120 nm-thick) grown in $P_O = 1 \times 10^{-1}$ mbar is still under epitaxial strain of $\varepsilon_x \approx +0.5\%$. This further suggests that the low-temperature film growth prevents oxygen diffusion/reorganization in the film. In contrast, it was found that the in-plane parameter relaxes toward the bulk value (Gd 20%, $a = 5.425$ Å) [1] and the out-of-plane c-axis expands with $\varepsilon_z \approx +0.72\%$ when lowering the P_O (figure 2(b)). Thus, the reduced CGO films are tetragonally distorted, verified by measuring their asymmetric {024} planes at four different φ angles (0°, 90°, 180°, and 360°) in XRD. However, the CGO peak position no longer shifted with further increase in the reduction condition ($P_O \leqslant 5 \times 10^{-3}$ mbar), as shown in figure 2(d), probably reaching a limited V_O concentration under the given growth condition.
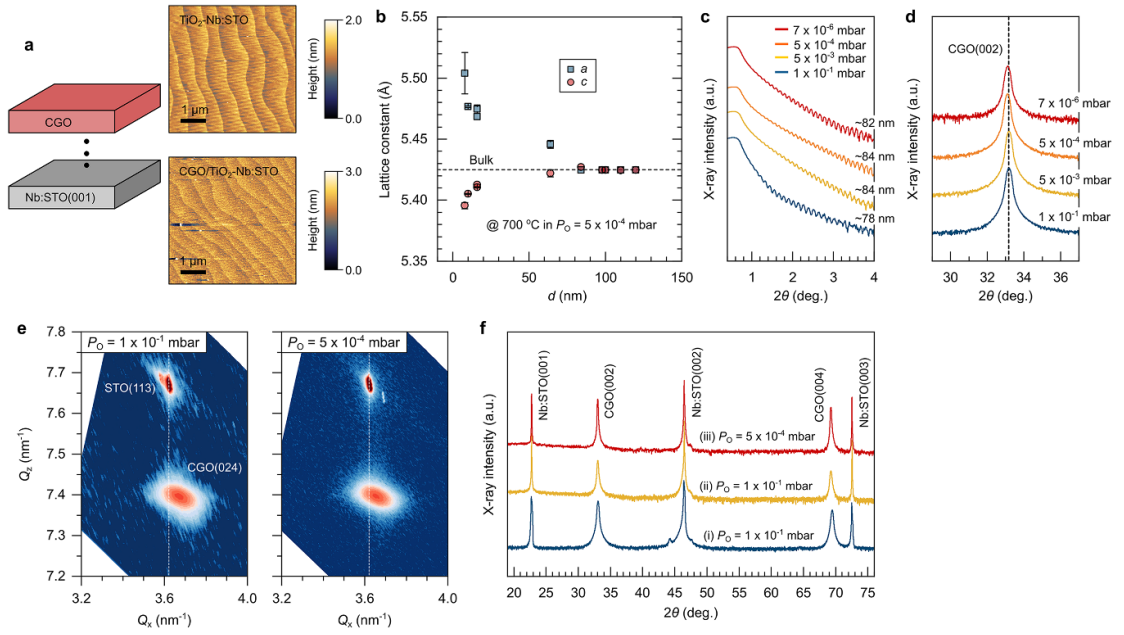
Figure 1. Epitaxial growth of CGO(001) films on Nb:STO(001) at 700 °C. (a) AFM topography images ($5 \times 5 \ \mu m^2$) before (upper) and after (lower) CGO film growth on TiO$_2$-terminated STO(001) substrate. The film was grown at $P_O = 5 \times 10^{-4}$ mbar. (b) a- and c-lattice parameters of the CGO films as a function of thickness, d, grown at $P_O = 5 \times 10^{-4}$ mbar. (c) X-ray reflectivity profiles for the grown CGO films. (d) XRD θ–2θ CGO(002) scans for the films as a function of P_O. (e) RSM CGO(024) reflections near Nb:STO(113) for the films grown in $P_O = 1 \times 10^{-1}$ mbar and 5×10^{-4} mbar. (f) XRD θ–2θ scans for the epitaxial CGO films grown at different places: (i) a CGO(001) film on Nb:STO(001) in 1×10^{-1} mbar at DTU, (ii) a CGO(001) film on Nb:STO(001) in 1×10^{-1} mbar at MLU, and (iii) a CGO (001) film on Nb:STO(001) at $P_O = 5 \times 10^{-4}$ mbar at MLU.
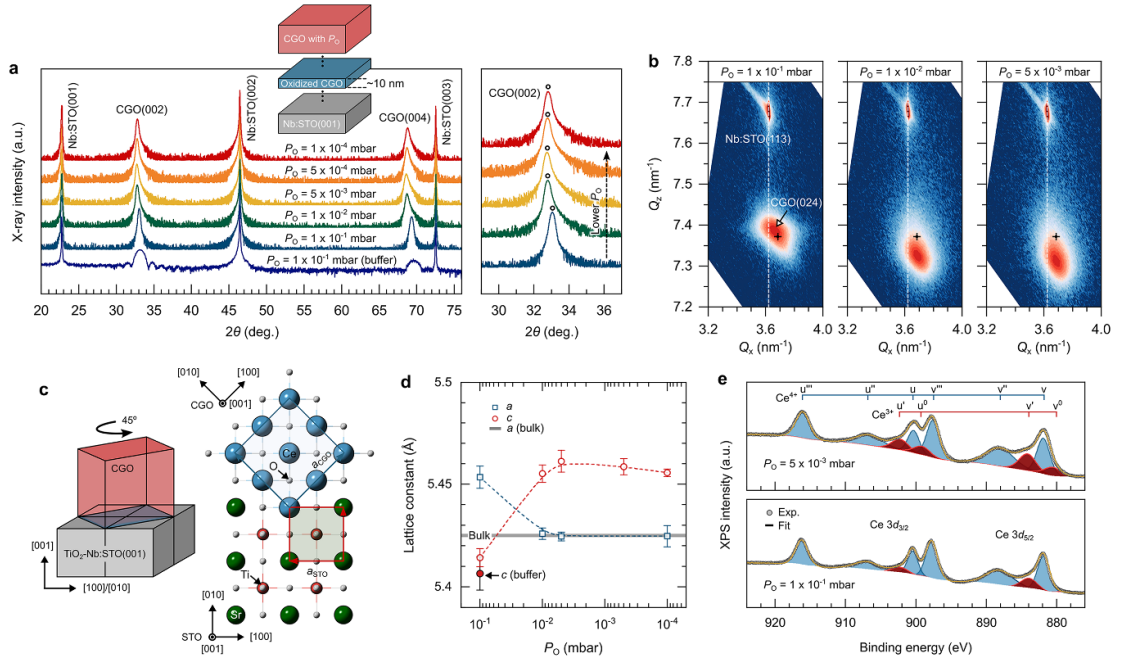

Figure 2. A two-step growth of epitaxial CGO films. (a) XRD θ–2θ scans for the CGO(001) films as a function of P_O (1×10^{-4} to 1×10^{-1} mbar), grown on CGO(001) buffer layer/TiO$_2$-terminated Nb:STO(001). Schematics show a two-step film growth: (i) an initial growth of 10 nm-thick oxidized buffer layer at $T = 700$ °C and (ii) the subsequent 100 nm-thick film growth at $T = 400$ °C. The right panel shows the variations in the XRD CGO(002) peak position of the films. (b) RSM CGO(024) reflections near STO(113) reflection. The cross bar indicates a reference CGO(024) reflection, based on a lattice parameter of bulk Ce$_{0.8}$Gd$_{0.2}$O$_{1.90}$ ($a = 5.425$ Å). (c) Schematics for the epitaxial relationship between CGO and Nb:STO as [110]$_{CGO}$||[100]$_{Nb:STO}$ and [001]$_{CGO}$||[001]$_{Nb:STO}$. The right panel represents the in-plane lattice alignment between the CGO and Nb:STO. (d) Variations in the a- and c-lattice parameters of the grown CGO films as a function of P_O. (e) XPS Ce $3d$ core level spectra for the CGO films grown at $P_O = 1 \times 10^{-1}$ mbar (lower) and 5×10^{-3} mbar (upper).
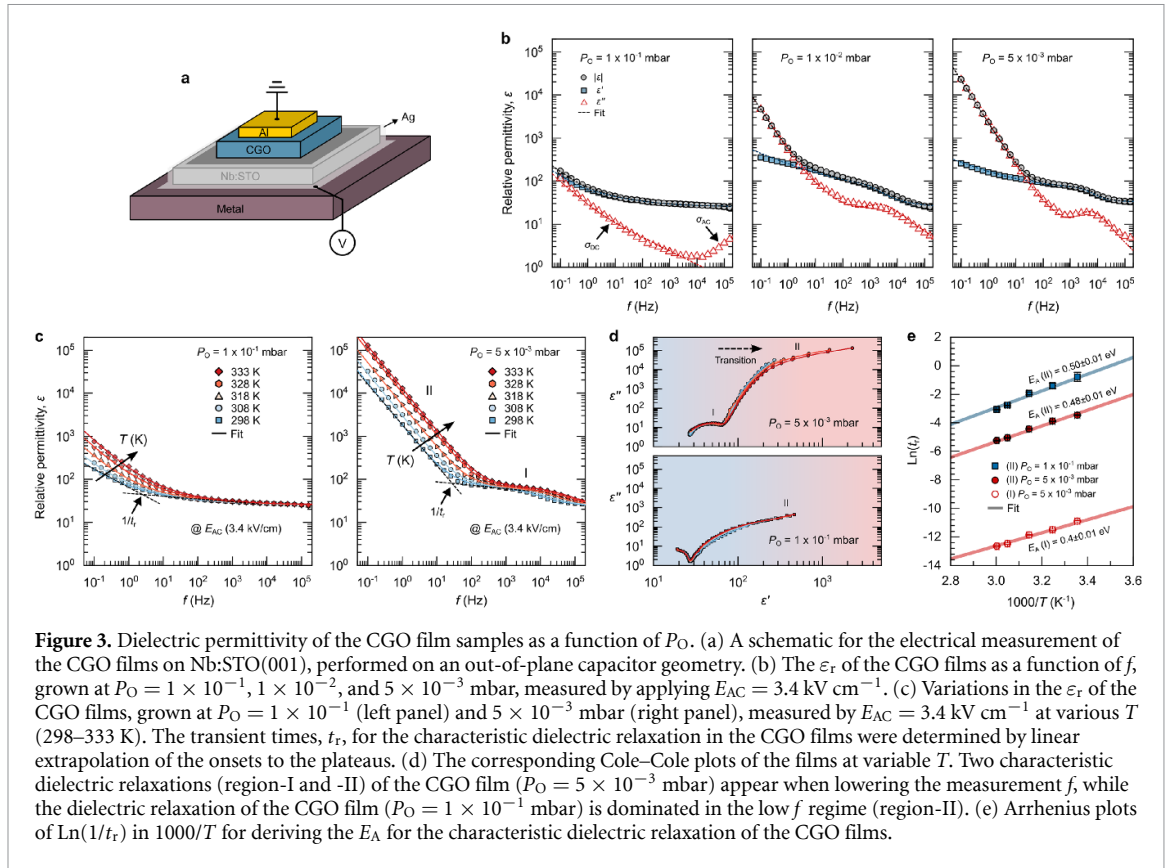
Figure 3. Dielectric permittivity of the CGO film samples as a function of P_O. (a) A schematic for the electrical measurement of the CGO films on Nb:STO(001), performed on an out-of-plane capacitor geometry. (b) The ε_r of the CGO films as a function of f, grown at $P_O = 1 \times 10^{-1}$, 1×10^{-2}, and 5×10^{-3} mbar, measured by applying $E_{AC} = 3.4$ kV cm^{-1}. (c) Variations in the ε_r of the CGO films, grown at $P_O = 1 \times 10^{-1}$ (left panel) and 5×10^{-3} mbar (right panel), measured by $E_{AC} = 3.4$ kV cm^{-1} at various T (298–333 K). The transient times, t_r, for the characteristic dielectric relaxation in the CGO films were determined by linear extrapolation of the onsets to the plateaus. (d) The corresponding Cole–Cole plots of the films at variable T. Two characteristic dielectric relaxations (region-I and -II) of the CGO film ($P_O = 5 \times 10^{-3}$ mbar) appear when lowering the measurement f, while the dielectric relaxation of the CGO film ($P_O = 1 \times 10^{-1}$ mbar) is dominated in the low f regime (region-II). (e) Arrhenius plots of Ln($1/t_r$) in 1000/T for deriving the E_A for the characteristic dielectric relaxation of the CGO films.

The observed out-of-plane lattice expansion could be attributed to the inclusion and/or preferential ordering/accumulation of V_O along the (001) direction of the CGO(001) films, leading to a tetragonal distortion. The preferential out-of-plane lattice expansion was further confirmed by growing the same low-temperature CGO film layer ($\sim$120 nm) on a CGO buffer ($\sim$10 nm)/SRO ($\sim$15 nm)/Nb:STO(001) (see supplementary figure S2). Similar tetragonal lattice distortion was observed in ceria, characterized by a cubic (space group: *Fm-3m*) to tetragonal (*P4$_2$/nmc*) phase transition with approximately 1.3% volume expansion [27]. Further, this phase transition is expected to be promoted and stabilized with a high V_O concentration due to the associated stress, driven by the change in the host cation radii, i.e., Ce^{4+} (97 pm) $\rightarrow$ Ce^{3+} (114 pm). To verify the changes in the oxidation state of Ce, we performed XPS measurements for the CGO films, grown at $P_O = 1 \times 10^{-1}$ and 5×10^{-3} mbar. Figure 2(e) illustrates the Ce 3d core level spectra for the films. The spectral fittings include the six peaks (v, v'', v''', u, u'', u''') and four peaks (v^0, v', u^0, u'), corresponding to three pairs of spin–orbit doublets for the Ce^{4+} valence state and two pairs of doublets for the Ce^{3+} state, respectively [28]. Clearly, we found that the surface of the film grown at $P_O = 5 \times 10^{-3}$ mbar possesses a higher Ce^{3+} concentration [Ce^{3+}/(Ce^{3+}+Ce^{4+}) = 25.1 ± 1.2%], compared to the grown film at $P_O = 1 \times 10^{-1}$ mbar, which has a concentration of 11.3 ±1.3%. The corresponding surface oxygen deficiency, δ, of the Gd$_{0.2}$(Ce$^{3+/4+}$)$_{0.8}$O$_{2-\delta}$ films were determined to be $\approx$11.33% ($P_O = 1 \times 10^{-1}$ mbar) and $\approx$25.1% ($P_O = 5 \times 10^{-3}$ mbar), respectively, corresponding to a larger excess V_O content ($\approx$12.5%) in the grown film at the lower P_O. Note that these XPS results only indicates a tendency for the V_O formation in the film with P_O as the probing depth is limited to the surface of the films. Hence, our results qualitatively suggest that the tetragonal CGO(001) films with the out-of-plane expansion are stabilized by a high V_O concentration, together with the concentration (10%) induced by 20% trivalent Gd doping.
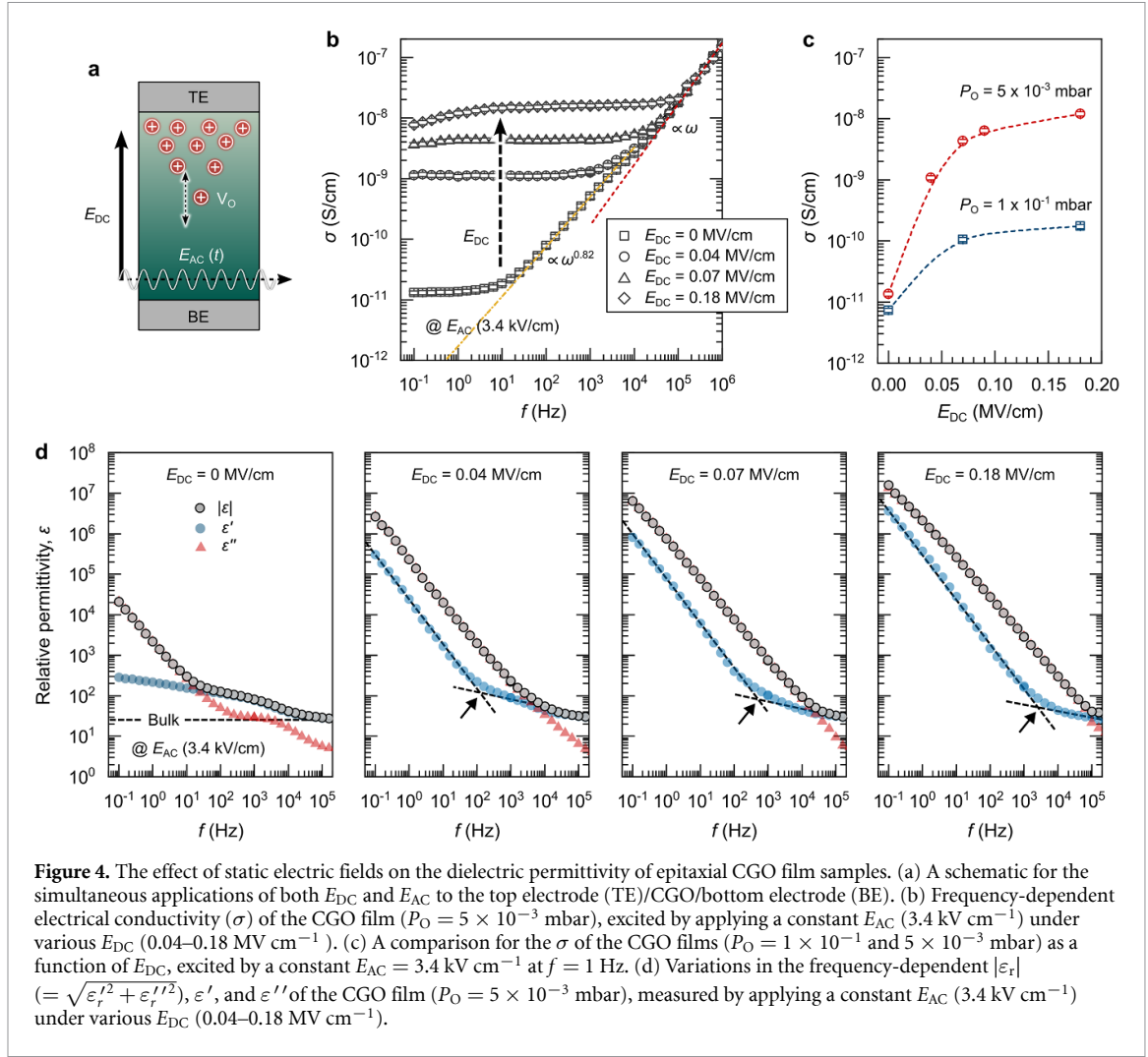
To investigate the effect of V_O concentration on the electrical and dielectric properties of the CGO films grown at different P_O, we performed impedance spectroscopy measurements. Sputtered Al (approximately 100 nm) was used as top electrode on all the film samples and the electrical measurements were performed in out-of-plane capacitor geometry as schematically illustrated in figure 3(a). To eliminate possible external effects (e.g. an interfacial effect between the CGO film and Nb:STO substrate or a dielectric response of substrate), all the side walls of Nb:STO substrates were electrically shorted to a bottom metal plate with conductive Ag paste. Moreover, no interfacial effects were found when compared two samples, CGO/Nb:STO and CGO/SRO/Nb:STO, showing almost identical electrical/dielectric responses (see the supplementary figure S3). The real part $\varepsilon'(\omega)$ and imaginary part $\varepsilon''(\omega)$ of the permittivity were derived from the

measured complex impedance [$Z^*(\omega) = Z'(\omega) + jZ''(\omega)$, where $\omega \, (= 2\pi f)$ is the angular frequency] in a conventional way. Details of the calculations and data fitting functions are given in the Experimental section.

Figure 3(b) shows the complex apparent dielectric permittivity of the CGO film samples grown at different P_O (1×10^{-1}, 1×10^{-2} mbar, and 5×10^{-3} mbar), measured by applying a constant alternating electric field ($E_{AC} = 3.4$ kV cm^{-1}) across a range of f from 100 mHz to 200 kHz. The results indicate a significant increase in the relative permittivity ($|\varepsilon_r| = \sqrt{\varepsilon'^2 + \varepsilon''^2}$) of the films when $f \to 0$, while remaining high frequency permittivity (ε') of 25–28. Clearly, this feature is further obvious with the films grown at $P_O < 1 \times 10^{-1}$ mbar showing a strong frequency dependence with two prominent dielectric relaxation behaviors: (I) in the high frequency (100 Hz $< f <$ 10 kHz) region, the ε' is around 70–100, which is certainly larger than the intrinsic high-frequency dielectric constant ($\varepsilon_\infty \sim$20–30) of CGO and similar oxides, and (II) in the low frequency regime ($f <$ 100 Hz), the permittivity considerably increases ($|\varepsilon_r| > 10^4$) following a power law [$\propto \omega^{-(1-s)}$, where s is a dimensionless exponent [29, 30]. Thus, two main contributions were considered to describe the observed dielectric response of the CGO films grown at relatively lower P_O. The high-frequency dielectric response in the region (I) could reflect the conductivity difference between the relatively oxidized buffer and reduced film layer. These two elements lead to a Debye-like relaxation with a peak loss at $\sim$2–5 kHz, based on charge accumulation at the interface with different carrier relaxation times (τ) in the two film layers, which stands for the releasing time of excess carriers across the interface [31]. In this regime, the interface capacitance is larger than the capacitance of the film layers. Once the interfacial conductivity becomes comparable with or smaller than the conductivity of the film layer, the loss (ε'') increases toward lower frequencies as seen in figure 3(b). This is the so-called MW relaxation. In fact, this feature is absent in the film grown at $P_O = 1 \times 10^{-1}$ mbar as the conductivity of the two layers (buffer and film) are similar. On the other hand, we found an increase in both the ε' and ε'' of all the films when lowering f, but with different relaxation times. This is dissimilar to typical Debye-type dipolar or MW relaxation models, which lead to a ε' plateau and an increase in ε'' with a slope of $\propto \omega^{-1}$ with decreasing f. If the exponent $s < 1$ (in equation (6.2)), it is an indication for the contribution of hopping conduction to the dielectric relaxation, which is associated with ionic migration within the CGO films, described by *Jonscher*'s UDR [29]. Thus, the conductivity of the CGO system can be described as $\sigma(\omega) = \sigma_{DC} + \sigma_U \omega^s$, where σ_{DC} is the dc conductivity and σ_U is the hopping conductivity. Based on these, we employed complex dielectric functions for data fittings describing the two dominant relaxations, MW and UDR (see the Experimental section). Our fitting results indicate the largely increased ε'' and a faster relaxation toward higher frequencies due to the increased $\sigma(\omega)$ of the samples grown at lower P_O. This implies the presence of a higher concentration of mobile V_O species in the samples ($P_O < 1 \times 10^{-1}$ mbar), confirmed by XRD and XPS.

To further understand such relaxation behaviors, we performed the permittivity measurements for the two samples ($P_O = 1 \times 10^{-1}$ and 5×10^{-3} mbar) at various temperatures (T = 298–333 K) (figure 3(c)). We found that the two samples show different relaxation behaviors: the film grown at $P_O = 1 \times 10^{-1}$ mbar only shows relaxation (II) over the measured f range due to the absence of MW effect, while the film grown at $P_O = 5 \times 10^{-3}$ mbar shows two types of relaxation (I) and (II). The transition time (t_r) for the characteristic dielectric relaxation of the samples was determined by linear extrapolation of the onsets to the relative plateaus. Interestingly, the t_r shifts toward higher frequencies with a continuous increase in both the ε' and ε'' when increasing T (figure 3(d)), indicating that the ionic conduction also contributes an increase in the space charge polarization of the system. Figure 3(e) shows the Arrhenius plots of Ln(t_r) in 1000/T. The activation energy, E_A (I), of the t_r for the high frequency dielectric relaxation (I) was determined to be 0.40 ± 0.01 eV for $P_O = 5 \times 10^{-3}$ mbar. This could be predominantly associated with polarons hopping as an ionic conduction is limited at the high frequency regime [32]. The E_A (II) of the t_r for the relaxation (II) was determined to be 0.50 ± 0.01 eV and 0.48 ± 0.01 eV for $P_O = 1 \times 10^{-1}$ mbar and 5×10^{-3} mbar, respectively [1, 33]. The CGO films grown at lower P_O possess the compensating oxygen vacancies (5% of oxygen sites due to the 20% Gd dopants on Ce sites) and additional oxygen vacancies (y), which stem from a reducing process step in the film growth (see figure 2) [34]. The complete formula can be written in the Kröger–Vink notation as $Ce^\times_{0.8-2y}Ce'_{2y}(Gd'_{Ce})_{0.2}Ce^\times_{1.9-y}(V_O^{\bullet\bullet})_{0.1+y}$. The activation energy for the V_O hopping is in a range of 0.45–0.70 eV in undoped CeO$_{2-x}$, strongly dependent on environmental conditions and the microstructure [32, 33, 35]. In doped ceria with 20% Gd, this value increases to 0.75 eV due to the trapping of $V_O^{\bullet\bullet}$ near the Gd dopants [33]. Hence, the excess V_O (y) compensated by Ce^{3+} can be more mobile than those associated with Gd, resulting in a large increase in the permittivity of the reduced CGO films with lower E_A [1]. Thus, when an electric field is applied to the sample at the low frequency regime, a macroscopic/long-range charge separation may appear as the $V_O^{\bullet\bullet}$ and the small polarons ($4f$ electron of Ce^{3+}) are diffusing along the field. Both have similar activation energies of approximately 0.5 eV.

Our observations suggest that the ionic conductivity of the system is key for tailoring the permittivity of the CGO system. We conducted the impedance measurements for the film sample ($P_O = 5 \times 10^{-3}$ mbar), excited by combined electric fields, simultaneous applications of a constant driving AC field ($E_{AC} = 3.4$ keV)

Figure 4. The effect of static electric fields on the dielectric permittivity of epitaxial CGO film samples. (a) A schematic for the simultaneous applications of both E_{DC} and E_{AC} to the top electrode (TE)/CGO/bottom electrode (BE). (b) Frequency-dependent electrical conductivity (σ) of the CGO film ($P_O = 5 \times 10^{-3}$ mbar), excited by applying a constant E_{AC} (3.4 kV cm^{-1}) under various E_{DC} (0.04–0.18 MV cm^{-1}). (c) A comparison for the σ of the CGO films ($P_O = 1 \times 10^{-1}$ and 5×10^{-3} mbar) as a function of E_{DC}, excited by a constant $E_{AC} = 3.4$ kV cm^{-1} at $f = 1$ Hz. (d) Variations in the frequency-dependent $|\varepsilon_r|$ ($= \sqrt{\varepsilon_r'^2 + \varepsilon_r''^2}$), ε', and ε'' of the CGO film ($P_O = 5 \times 10^{-3}$ mbar), measured by applying a constant E_{AC} (3.4 kV cm^{-1}) under various E_{DC} (0.04–0.18 MV cm^{-1}).

under different static fields ($E_{DC} = 0.04$, 0.07, and 0.18 MV cm^{-1}) as schematically illustrated in figure 4(a). Firstly, we examined the $\sigma(\omega)$ of the CGO film sample over a frequency range of 100 mHz–1 MHz (figure 4(b)). When the E_{AC} was applied to the sample, it shows an ionic relaxation behavior at $f < 5$ kHz, expressed by $\sigma \propto \omega^{0.82}$ [1]. The exponent range of $0 < s < 1$ represents dispersive ionic diffusion, while at $f > 5$ kHz a universal limiting ac-conductivity was found with $\sigma \propto \omega$ [36]. Importantly, a large increase in the $\sigma(\omega)$ was found with $s \rightarrow 0$ when simultaneously increasing the E_{DC}. This indicates the occurrence of frequency-independent dc-conductivity, indicating greatly enhanced long-range ionic diffusion or hopping process [37]. The static field-enhanced ionic conductivity is further signified with the level of excess V_O when comparing the two samples ($P_O = 1 \times 10^{-1}$ and 5×10^{-3} mbar) as shown in figure 4(c). Figure 4(d) exhibits the frequency dependent dielectric permittivity of the CGO film ($P_O = 5 \times 10^{-3}$ mbar) as a function of E_{DC}. Notably, as the E_{DC} increases (up to 0.18 MV cm^{-1}), we observed a large increase in both the ε' ($\approx 10^6$) and ε'' ($\approx 10^7$) of the film at low frequencies ($f < 1$ Hz). Moreover, higher E_{DC} strength effectively shifts the t_r toward high frequencies ($f > 1$ kHz). These observations are consistent with our previous result [1]. The enhanced V_O hopping/conduction in the system is associated with lowered activation energies when the static fields are applied. Consequently, our results show that the dielectric permittivity of the single crystalline CGO films strongly depends on the activation energy of V_O hopping and its frequency dependence under static field applications, which can be effectively tuned by incorporating excess V_O. However, we found that effective ionic conduction for the emergence of large permittivity in single crystalline CGO films can be driven by a much smaller E_{DC} strength (e.g. 0.18 MV cm^{-1}) than that required for polycrystalline films (e.g. 1 MV cm^{-1}). This could be due to higher excess V_O concentration and facilitated hopping by the absence of microstructural or other external effects (e.g., grain boundaries).

4. Summary

In conclusion, we demonstrate an effective way to control the V_O content in epitaxial CGO(001) films grown on Nb:STO(001). Our findings show that oxygen reduction in the epitaxial CGO films is limited during high-temperature growth. In contrast, the two-step growth effectively induces excess V_O in the single crystalline CGO(001) films, stabilizing tetragonal CGO films with a preferential out-of-plane lattice expansion. Subsequently, we found that controlling excess V_O contents is essential for the emergence of giant apparent dielectric permittivity (e.g. $\varepsilon' \approx 10^6$) of the system, which can be effectively tuned by simultaneous static electric field applications, potentially enabling the generation of substantial electromechanical coupling and piezoelectric effects. Therefore, this work provides crucial insights for designing fluorites or similar oxides using ionic defects for use in energy-efficient applications such as electromechanical and energy storage devices.

Data availability statement

All data that support the findings of this study are included within the article (and any supplementary files).

Acknowledgments

Conflict of interest

The authors declare no conflict of interest.

ORCID iDs

A Palliotto ⦾ https://orcid.org/0009-0003-0310-8113
A D Rata ⦾ https://orcid.org/0000-0003-2244-4908
A Herklotz ⦾ https://orcid.org/0000-0002-1545-131X
S Zhou ⦾ https://orcid.org/0000-0002-4885-799X
D-S Park ⦾ https://orcid.org/0000-0001-9212-7516

References

[1] Park D-S *et al* 2022 Induced giant piezoelectricity in centrosymmetric oxides *Science* **375** 653–7
[2] Waser R and Aono M 2007 Nanoionics-based resistive switching memories *Nat. Mater.* **6** 833–40
[3] Park D-S *et al* 2020 The emergence of magnetic ordering at complex oxide interfaces tuned by defects *Nat. Commun.* **11** 3650
[4] Park D-S *et al* 2018 Electromagnetic functionalization of wide-bandgap dielectric oxides by boron interstitial doping *Adv. Mater.* **30** 1802025
[5] Park D-S *et al* 2023 Controlled electronic and magnetic landscape in self-assembled complex oxide heterostructures *Adv. Mater.* **35** 2300200
[6] Goodenough J B and Park K-S 2013 The Li-ion rechargeable battery: a perspective *J. Am. Chem. Soc.* **135** 1167–76
[7] Lee J G, Park J H and Shul Y G 2014 Tailoring gadolinium-doped ceria-based solid oxide fuel cells to achieve 2 W cm^{-2} at 550 °C *Nat. Commun.* **5** 4045
[8] Kim Y-M, He J, Biegalski M D, Ambaye H, Lauter V, Christen H M, Pantelides S T, Pennycook S J, Kalinin S V and Borisevich A Y 2012 Probing oxygen vacancy concentration and homogeneity in solid-oxide fuel-cell cathode materials on the subunit-cell level *Nat. Mater.* **11** 888–94
[9] Tuller H L and Bishop S R 2011 Point defects in oxides: tailoring materials through defect engineering *Annu. Rev. Mater. Res.* **41** 369
[10] Korobko R, Patlolla A, Kossoy A, Wachtel E, Tuller H L, Frenkel A I and Lubomirsky I 2012 Giant electrostriction in Gd-doped ceria *Adv. Mater.* **24** 5857–61
[11] Yavo N, Smith A D, Yeheskel O, Cohen S, Korobko R, Wachtel E, Slater P R and Lubomirsky I 2016 Large nonclassical electrostriction in (Y, Nb)-stabilized δ-Bi$_2$O$_3$ *Adv. Funct. Mater.* **26** 1138–42
[12] Chen B *et al* 2018 Large electrostrictive response in lead halide perovskites *Nat. Mater.* **17** 1020–6
[13] Yu J and Janolin P-E 2022 Defining "giant" electrostriction *J. Appl. Phys.* **131** 170701
[14] Newnham R E, Sundar V, Yimnirun R, Su J and Zhang Q M 1997 Electrostriction: nonlinear electromechanical coupling in solid dielectrics *J. Phys. Chem.* B **101** 10141–50
[15] Yavo N, Yeheskel O, Wachtel E, Here D, Frenkel A I and Lubomirsky I 2018 Relaxation and saturation of electrostriction in 10 mol% Gd-doped ceria ceramics *Acta Mater.* **144** 411–8
[16] Gopal C B *et al* 2017 Equilibrium oxygen storage capacity of ultrathin CeO$_{2-\delta}$ depends non-monotonically on large biaxial strain *Nat. Commun.* **8** 15360

[17] Yang N *et al* 2017 Effect of dopant ionic radius on cerium reduction in epitaxial cerium oxide thin films *J. Phys. Chem.* C **121** 8841–9

[18] Yang G, El Loubani M, Chalaki H R, Kim J, Keum J K, Rouleau C M and Lee D 2023 Tuning ionic conductivity in fluorite Gd-doped CeO_2-Bixbyite RE_2O_3 (RE = Y and Sm) multilayer thin films by controlling interfacial strain *ACS Appl. Electron. Mater.* **5** 4556–63

[19] Mos R B, Petrisor T Jr, Nasui M, Calleja A, Puig T, Ciontea L and Petrisor T 2014 Enhanced structural and morphological properties of Gd-doped CeO_2 thin films obtained by polymer-assisted deposition *Mater. Lett.* **124** 306–9

[20] Chen Y, Pryds N, Schou J and Linderoth S 2011 Epitaxial growth of atomically flat gadolinia-doped ceria thin films by pulsed laser deposition *Appl. Phys.* A **105** 697–701

[21] Hofmann S 2011 *Auger- and x-ray Photoelectron Spectroscopy in Materials Science* (Springer)

[22] Scofield J 1976 Hartree–Slater subshell photoionization cross-sections at 1254 and 1487 eV *J. Electron Spectrosc. Relat. Phenom.* **8** 129–37

[23] Feng Z A, El Gabaly F, Xiaofei Y, Shen Z-X and Chueh W C 2014 Fast vacancy-mediated oxygen ion incorporation across the ceria–gas electrochemical interface *Nat. Commun.* **5** 4374

[24] Ma Y, Burye T E and Nicholas J D 2021 Pt current collectors artificially boosting praseodymium doped ceria oxygen surface exchange coefficients *J. Mater. Chem.* A **9** 24406–18

[25] Lee K-M, Brito M, DeCoster J, Linskens K, Mehdi K, Kim E, Kim H, Kwon G and Kim T J 2022 Influence of oxidizing and reducing pretreatment on the catalytic performance of CeO_2 for CO oxidation *J. Mol. Catal.* **528** 112465

[26] Morales M, Roa J J, Capdevila X G, Segarra M and Piñol S 2010 Mechanical properties at the nanometer scale of GDC and YSZ used as electrolytes for solid oxide fuel cells *Acta Mater.* **58** 2504–9

[27] Zhu H *et al* 2018 Charge transfer drives anomalous phase transition in ceria *Nat. Commun.* **9** 5063

[28] Mullins D R, Overbury S H and Huntley D R 1998 Electron spectroscopy of single crystal and polycrystalline cerium oxide surfaces *Surf. Sci.* **409** 307–19

[29] Jonscher A K 1977 The 'universal' dielectric response *Nature* **267** 673–9

[30] Nowick A S, Vaysleyb A V and Kuskovsky I 1998 Universal dielectric response of variously doped CeO_2 ionically conducting ceramics *Phys. Rev.* B **58** 8398

[31] Von Hippel A R 1954 *Dielectrics and Waves* (MIT Press)

[32] Kek-Merl D, Lappalainen J and Tuller H L 2006 Electrical properties of nanocrystalline CeO_2 thin films deposited by in-situ pulsed laser deposition *J. Electrochem. Soc.* **153** J15- J20

[33] Faber J, Geoffroy C, Roux A, Sylvestre A and Abélard A 1989 A systematic investigation of the dc electrical conductivity of rare-earth doped ceria *Appl. Phys.* A **49** 225–32

[34] Hadad M, Ashraf H, Mohanty G, Sandu C and Muralt P 2016 Key-features in processing and microstructure for achieving giant electrostriction in gadolinium doped ceria thin films *Acta Mater.* **118** 1–7

[35] Tschope A and Birringer R 2001 Grain size dependence of electrical conductivity in polycrystalline cerium oxide *J. Electroceram.* **7** 169–77

[36] Lee W K, Liu J F and Nowick A S 1991 Limiting behavior of AC conductivity in ionically conducting crystals and glasses: a new universality *Phys. Rev. Lett.* **67** 1559–61

[37] Garcia-Barriocanal J, Rivera-Calzada A, Varela M, Sefrioui Z, Iborra E, Leon C, Pennycook S J and Santamaria J 2008 Colossal ionic conductivity at interfaces of epitaxial ZrO_2:Y_2O_3/$SrTiO_3$ heterostructures *Science* **321** 676–80